Lab on a Chip

Accepted Manuscript

This is an *Accepted Manuscript*, which has been through the Royal Society of Chemistry peer review process and has been accepted for publication.

Accepted Manuscripts are published online shortly after acceptance, before technical editing, formatting and proof reading. Using this free service, authors can make their results available to the community, in citable form, before we publish the edited article. We will replace this *Accepted Manuscript* with the edited and formatted *Advance Article* as soon as it is available.

You can find more information about *Accepted Manuscripts* in the Information for Authors.

Please note that technical editing may introduce minor changes to the text and/or graphics, which may alter content. The journal's standard Terms & Conditions and the Ethical guidelines still apply. In no event shall the Royal Society of Chemistry be held responsible for any errors or omissions in this *Accepted Manuscript* or any consequences arising from the use of any information it contains.

ROYAL SOCIETY OF CHEMISTRY

www.rsc.org/loc

The deposition of asphaltenes in porous media, an important problem in science and macromolecular engineering, was for the first time investigated in a transparent packed-bed microreactor with online analytics that generated high-throughput information.

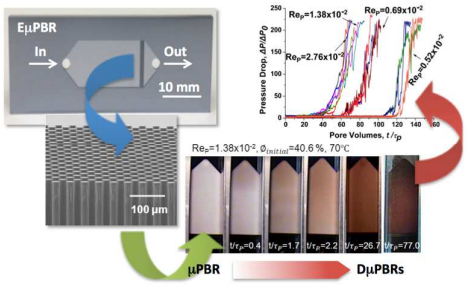

Lab on a Chip Accepted Manuscript

Lab on a Chip

RSCPublishing

PAPER

Microfluidic investigation of the deposition of asphaltenes in porous media

Cite this: DOI: 10.1039/x0xx00000x

Chuntian Hu, James E. Morris, and Ryan L. Hartman*

Received 00th January 2012,
Accepted 00th January 2012

DOI: 10.1039/x0xx00000x

www.rsc.org/

The deposition of asphaltenes in porous media, an important problem in science and macromolecular engineering, was for the first time investigated in a transparent packed-bed microreactor (μPBR) with online analytics to generate high-throughput information. Residence time distributions of the μPBR before and after loading with ~29μm quartz particles were measured using inline UV-Vis spectroscopy. Stable packings of quartz particles with porosity of ~40% and permeability of ~500mD were obtained. The presence of the packing materials reduced dispersion under the same velocity *via* estimation of dispersion coefficients and the Bodenstein number. Reynolds number was observed to influence the asphaltene deposition mechanism. For larger Reynolds numbers, mechanical entrapment likely resulted in significant pressure drops for less pore volumes injected and less mass of asphaltenes being retained under the same maximum dimensionless pressure drop. The innovation of packed-bed microfluidics for investigations on asphaltene deposition mechanisms could contribute to society by bridging macromolecular science with microsystems.

Introduction

Miniaturization has broadly advanced the physical and chemical rate principles of organic chemistry, in large part, by providing high-throughput knowledge that bridges molecular-level and laboratory-scale understandings. The ultimate goal of integrating online analytical analyses with microscale devices that yield directly scalable knowledge to real-world scenarios, albeit maturing, remains a vital limitation of the field. High molecular weight aromatics, such as asphaltenes, are difficult to characterise because of the complexity of their chemistry. Deciphering the science of such macromolecular aromatics impacts the sustainability of upstream conventional and unconventional energy production, chemicals manufacture, transportation systems, and the residential and commercial building industries. Tremendous potential exists for lab-on-a-chip devices to discover science that directly scales-up to make societal contributions.

Asphaltenes are macromolecular aromatics, and similar to amino acid derived macromolecules (*e.g.*, proteins, DNA, etc.) they are challenging to characterise due to their thermodynamic and functional complexities. They are the most complex component of crude oil. As a result, asphaltenes are commonly defined as the toluene-soluble, light n-alkanes-insoluble component of a specific crude oil or other carbonaceous materials such as bitumen and coal[1, 2]. They are the heaviest and most polarisable components. Asphaltenes obtained from crude oil using *n*-heptane as a precipitant are usually dark-coloured, fragile solids with C:H ratios of ~1:1.2 and specific gravity of ~1.2. They consist primarily of aromatic polycyclic clusters and heteroatoms (*e.g.*, N, S, O), as well as trace amount of metals such as V, Fe, and Ni. Similarities exist between asphaltenes and some lower molecular weight fine chemicals and pharmaceuticals. Merit exists for the green hydrothermal cracking of asphaltenes into fine chemical and pharmaceutical precursors. Even after decades of academic investigations, understandings of asphaltenes structures[2-11], behaviours at heterogeneous interfaces[10, 12-15], aggregation and solubility[4, 11, 16-26], precipitation and depositions[26-39], dissolutions[40-42], and the characterization of asphaltenes bearing media[37, 43-45], all remain essential topics of research in this important area of science.

Many factors, such as changes in the temperature, pressure, composition, and shear rate cause asphaltenes to precipitate and deposit on heterogeneous surfaces[1]. In upstream petroleum and natural gas production, instabilities of asphaltenes within subterranean porous media creates the potential to adversely affect production rates[46-48]. Two recognized models describe asphaltene deposition in porous media: adsorption and mechanical entrapment[47]. Adsorption is reversible with asphaltenes desorbing from siliceous and/or carbonate surfaces as their bulk concentrations decrease. Mechanical entrapment (*e.g.*, hydrodynamic bridging) is a physical blocking process of pore throats by precipitated asphaltene particles. Remediation techniques have been studied in order to understand how to mitigate the outcomes of either mechanism on production rates[49]. Conventional macroscale laboratory techniques, however, mask the intrinsic mechanisms and their relationship to asphaltene science.

Microfluidic systems allow for the precise control of conditions to study chemistry[50-57]. The high surface-to-volume ratios attainable in microscale devices and their reduced characteristic length scales within heterogeneous systems minimize the heat and mass transfer resistances, which suggests that microfluidic systems offer advantages in studying intrinsic

Lab on a Chip Accepted Manuscript

flow and reaction behaviour relative to conventional macroscopic systems[51]. The nature of porous media itself represents highly parallelized nanofluidic and microfluidic chemical reactors. Macroscale systems are commonly used to capture the science of chemical reactions in porous media, yet their non-invasive design overlooks key molecular and microscale, mechanistic information. Engineering packed-bed microreactors potentially creates a way to study chemical reactions in situ when unsteady-state time scales are magnitudes less than geological equilibrium conditions. The precipitation of asphaltenes in continuous flow, microchemical reactors[58-61], in our example, offers a novel approach to overcome the transport limitations while discovering the scalable nature of the kinetic parameters that characterise their deposition mechanisms in porous media.

In the present work, microfluidic devices were designed and fabricated in silicon and Pyrex, for the first time, to develop high-throughput understanding of the deposition of asphaltenes in porous media. Our quartz packed-bed microreactor with online analyses provides a ubiquitous platform to study the deposition of asphaltenes in micro-scale tortuous flows, which bridges the knowledge gap between molecular level events and macro-scale reservoir productions. The porosity loss and permeability impairment of the porous media before and after damages were also studied. The results of asphaltene deposition demonstrate packed-bed microreactors as promising microfluidic tools that could yield mechanistic understanding of high molecular weight aromatics for a broad cross-section of science.

Experimental

Chemicals

Toluene and acetone (HPLC grade) were obtained from EMD (Millipore, USA). Ethanol (absolute) and *n*-heptane (HPLC grade) were purchased from Alfa Aesar (Ward Hill, MA, USA). Quartz sand (30~40 mesh) was acquired from VWR International (West Chester, PA, USA). All liquids were used without further purification.

Device fabrication, layout, and analytics

Empty microreactors (EμPBR) were fabricated from 1mm polished single-crystal silicon wafers and capped with 1.1mm Pyrex wafers. The fabrication process primarily included photolithography (spin-coating, exposure, and development), deep reactive ion etching (DRIE), cleaning, anodically bonding of silicon wafers to Pyrex, and dicing into chips, as shown in Fig. S1a of the Electronic Supplementary Information (ESI)†. Fig. 1a illustrates a fabricated EμPBR with dimensions of 5.0x1.8x0.21cm. Here, the microchannel is 300μm in depth and 9mm in width. Near the outlet, 30 rows of cylindrical pillars of 20μm in diameter were etched 20μm apart, as depicted in the SEM micrograph of Fig. 1b. Quartz particle sizes were designed such that the largest particle size was less than one fourth of the minimum microchannel depth of 300μm to avoid aspect ratios that lead to bridging[61], *i.e.*, less than 75μm. The starting material, 30–40mesh quartz sands, was grinded by mortar and pestle in the presence of water. Particles were separated and collected using 635mesh and 500mesh sieves. The remaining ultrafine particles were removed by ultrasonic bath treatments. Microscope photographs, e.g., Fig. 1c. acquired using an optical microscope, were used to calculate the quartz particle size number distribution, as shown in Fig. 1d. From Fig. 1d, mean particle sizes of 29μm were estimated ranging from 17–38μm. The packed bed was prepared by injecting the ~29μm quartz particles dispersed in absolute ethanol into the EμR using a 5mL syringe. Fig. 1e shows the packaged system loaded with quartz particles, which creates a native packed-bed microreactor (μPBR). Fig. S1b further illustrates the underside fluidic connections the packaged system.

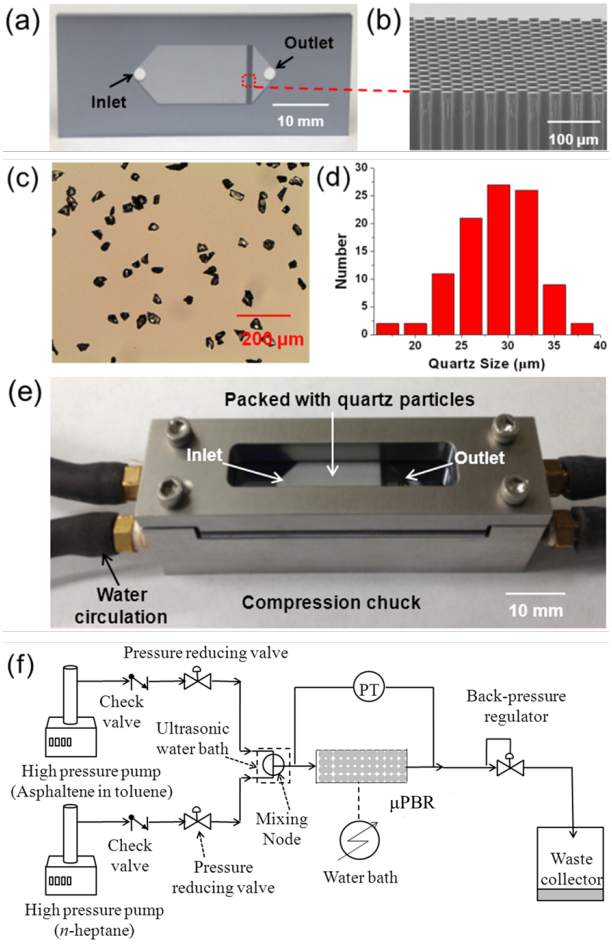

Fig. 1 (a) Photograph of the EμPBR with dimensions of 5.0x1.8x0.21cm. (b) SEM micrographs of 20μm pillars. (c) Microscope photograph and (d) estimated size distribution of the quartz particles. (e) Photograph of the packaged system with water circulation connections. (f) Schematic flow diagram of the experimental setup used to study the deposition of asphaltenes in the μPBR.

The experimental setup used to study asphaltene depositions is shown schematically in Fig. 1f. Two high-pressure pumps (Teledyne ISCO, Lincoln, NE, USA) were used to inject 4g/L asphaltene in toluene (40vol%) and *n*-heptane (60vol%) at constant flow rates. Inline check valves (IDEX Heath & Science, Oak Harbor, WA, USA) prevented back flows of the liquids. Two pressure-reducing valves (IDEX Heath & Science, Oak Harbor, WA, USA) were installed inline as relief devices. Asphaltenes dissolved in toluene and *n*-heptane were mixed in a stainless steel T-union within in an ultrasonic bath (VWR International, West Chester, PA, USA) to ensure no accumulations upstream of the μPBR. Inline pressure transducers (500psi, Honeywell Sensing & Control,

Lab on a Chip Accepted Manuscript

This journal is © The Royal Society of Chemistry 2014

Golden Valley, MN, USA), connected to the entrance and exit of the microreactor, enabled online analyses of pressure drops. The packaged μPBR interconnected to a heated circulating bath (Honeywell Sensing & Control, Golden Valley, MN, USA) maintained the μPBR temperature on-chip of 70.0℃. A 5psi back-pressure regulator (IDEX Heath & Science, Oak Harbor, WA, USA) maintained constant pressure at the μPBR outlet, and it established fluidic resistance in order to minimize the possibility of microchanneling within the μPBR.

Measurements of residence time distributions (RTDs)

Residence time distributions were measured using a continuous inline UV-Vis spectroscopy system, as shown in Fig. 2. As shown in Fig. 2a, a syringe pump (PHD 2000, Harvard Apparatus, Holliston, MA, USA) and 5mL SGE glass syringes were used to inject *n*-heptane (carrier solvent) at flow rates of 10.00, 20.00, 40.00, 80.00, and 160.0μL/min. A microscale injector (Fig. 2b, IDEX Heath & Science, Oak Harbor, WA, USA) with a 1.0μL sample loop of acetone (20vol% in *n*-heptane) delivered the tracer inline and upstream of the μPBR. Axial dispersion of the tracer was measured using inline UV-Vis spectroscopy (Fig. 2c, Ocean Optics, Dunedin, FL, USA) at the outlet of the μPBR. The peak absorbance wavelength of 277nm (Fig. 2d) was chosen to maximize the signal-to-noise ratio, which improved the resolution of dilute tracer concentration measurements. The microscale injector, packaged μPBR, and UV-Vis spectroscopy were interconnected by 0.005" tubing in order to reduce the dead volume. The light source was allowed to warm-up for at least 20min before performing RTD experiments.

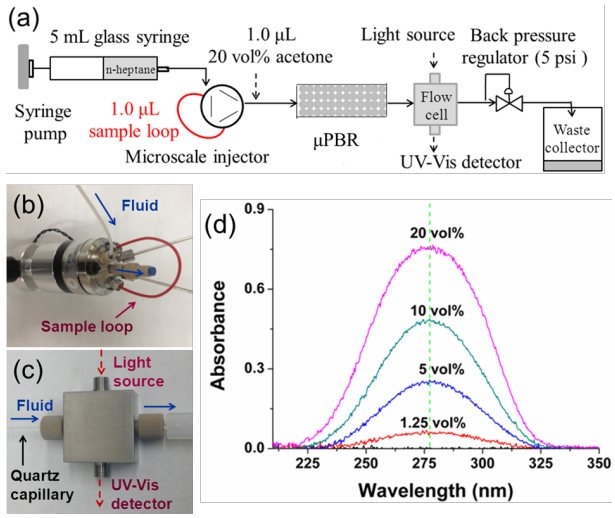

Fig. 2 (a) Schematic diagram of continuous inline UV-Vis spectroscopy used to obtain RTD measurements. (b) The microscale injector with a 1.0μL sample loop (8cm of 0.005" I.D. red tubing), and (c) flow cell integrated with a 400μm I.D. quartz capillary. (d) Measurements of the UV-Vis absorbance (at 277nm) of acetone in *n*-heptane for varying concentrations.

Preparation of asphaltenes

Asphaltenes used in the present study were the *n*-heptane insoluble fraction of a Wyoming crude oil deposit provided by Nalco Energy Services. The insoluble fraction was then dissolved in toluene. Passing the solution through a ceramic filter fitted with Whatman No.1 filter paper separated the insoluble organic and inorganic material. Next, *n*-heptane was combined with the filtrate, the insoluble material collected, and the procedure repeated until no asphaltenes precipitating out of the solution. The filtered asphaltene precipitates were then dried at 60.0 ℃ for 24hrs. The dried asphaltenes (dark-coloured, friable solids) were used in the present work.

Theoretical

Axial dispersion model

Residence time distribution theory and dispersion models in laminar flow microreactors have been previously described[62]. Under open-open boundary conditions a molecule can pass the boundary several times[63] and the system deviates from plug flow. The dimensionless residence time distribution function is given as[64, 65],

$$E(\theta) = \frac{1}{\sqrt{4\pi(D^*/uL)\theta}} exp\left[-\frac{(1-\theta)^2}{4(D^*/uL)\theta}\right] \quad (1)$$

where D^* is the dispersion coefficient, u the superficial velocity, and L the axial length of the microreactor. The maximum peak heights of $E(\theta)$ curves yield estimations of D^*, and hence the ratio of convection to diffusion (*i.e.*, the Bodenstein number, $Bo=ud_E/\mathcal{D}$) is estimated for known L/d_E ratios of magnitude 10^2 by combining into[64],

$$\mathcal{D} = \frac{u^2 d_E^2}{192D^*} \quad (2)$$

Here, d_E is the effective cross-sectional diameter of the microchannel, and $\mathcal{D}$ is the molecular diffusivity. Equations (1) and (2) characterise the extents of axial dispersion and molecular diffusion within μPBRs.

Porosity, permeability, and skin factor of porous media

In packed-beds, important parameters that characterize the porous media include the length of the packed-bed, L, the mean particle size, d_p, and the interstitial fluid velocity, u_i,

$$u_i = u/\emptyset \quad (3)$$

where u is the superficial velocity, and $\emptyset$ is the porosity of the porous media (*i.e.*, the void fraction).[66]

Permeability describes how well a given liquid flows through a porous media, and it is controlled by pore sizes and their interconnectivity. The one-dimensional empirical equation discovered by Darcy continues to be widely adopted by engineers and scientists in their descriptions of porous media[67]. Permeability can be estimated by Darcy's law[68],

$$Q = \frac{\kappa A}{\mu}\frac{\Delta P}{L} \quad (4)$$

which describes the relationship between the flow rate in porous media, Q (*e.g.*, m^3/s or barrels per day, bpd), the cross-sectional area normal to the axial direction of flow, A (m^2), the permeability, κ (m^2 or mD, and 1mD = $9.869233\text{x}10^{-16}\text{m}^2$), the dynamic viscosity of the fluid, μ ($Pa \cdot s$ or Cp), and the pressure drop across the packed-bed, ΔP (Pa or Psi).

In porous media, the presence of solid particles themselves causes the diffusion paths of molecules to deviate from their original trajectories. Tortuosity should be considered to

Lab on a Chip Accepted Manuscript

accurately estimate the role of porosity on diffusion, which is defined by[69, 70],

$$\mathcal{T} = \frac{L_e}{L_s} \quad (5)$$

where L_e and L_s are the actual length and the straight length of the molecule flow paths. Unlike $\emptyset$, $\mathcal{T}$ values are challenging to directly measure. An empirical tortuosity-porosity relationship for unconsolidated sands has previously been described by[70],

$$\mathcal{T}^2 = (A\emptyset^{1-m})^n \quad (6)$$

where the parameter values in Equation (6) are A=1, n=1 and m=2.14.

The hydraulic radius between the sand grains can be estimated by[71],

$$r_H = \frac{\emptyset}{(1-\emptyset)}\frac{d_P}{6} \quad (7)$$

where d_P is the mean particle size of the sand grains.

The dimensionless van Everdingen-Hurst Skin Factor, s, commonly used to describe the extent of subterranean well-bore damage, is defined as[71],

$$s = \Delta P \frac{7.08\kappa_{initial} h}{Q\mu} \quad (8)$$

where h is the thickness of production zone.

Reynolds number in a packed-bed, Re_P, is defined as[72],

$$Re_P = \frac{d_P u \rho}{(1-\emptyset)\mu_i} \quad (9)$$

where ρ is the density of the solvent. Fully laminar conditions exist for Re_P < 10, while fully turbulent from > 2000. Equations (3) through (9) characterise the extent asphaltene deposition within μPBRs has on fluid flow through the porous media.

Results and discussion

Porosity, permeability, and tortuosity of the μPBR

Characterisations of an EμPBR free of quartz particles were first performed to establish the dimensionless constraints that govern the microfluidic system. Table 1 summarizes the experimental conditions achieved in the EμPBR and the corresponding dimensionless quantity estimates based on 40vol% toluene and 60vol% *n*-heptane solvent injections. In empty reactors (Table 1a), Reynolds number ranged from 0.25 to 4.1, and as a consequence laminar flow was established for residence times ranging from 0.28 to 4.50min. Viscosities and densities of toluene and n-heptane at 70℃ were obtained from the work of others[73-76]. Capillary numbers ($Ca = \mu u/\gamma$, where γ is the interfacial tension of the liquid) were estimated on the order of 10^{-5}, while the Weber number ($We = d_E\rho u^2/\gamma$) ranged from 0.02 to 6.09 x10^{-5}. Therefore, surface tension dominated over the inertial forces within the EμPBR. The ratio of $Ca/Re=\mu^2/(d_E\rho\gamma)$ was estimated to be 0.37x10^{-5} (see Fig. S2), which is much smaller than a previously reported value of mineral oil-seawater systems[62] due to the small viscosity and larger effective microchannel diameter. Estimation of the same quantities of μPBRs required first understanding the porosity of the porous media.

Table 1. Experimental conditions and dimensionless quantity estimates for the EμPBR and μPBR.

		(I)	(II)	(III)	(IV)	(V)	(VI)
(a) EμPBR	Total flow rate, F_T (μL/min)	-	10.00	20.00	40.00	80.00	160.0
	Mean velocity, u (x10^{-4} m/s)	-	0.62	1.23	2.46	4.92	9.84
	Re	-	0.25	0.51	1.02	2.04	4.08
	Ca (x10^{-5})	-	0.09	0.19	0.38	0.76	1.52
	We (x10^{-5})	-	0.02	0.09	0.38	1.52	6.09
	τ (min)	-	4.50	2.25	1.13	0.56	0.28
(b) μPBR	Total flow rate, F_T (μL/min)	8.00	10.00	20.00	40.00	80.00	160.0
	Interstitial velocity, u_i (x10^{-4} m/s)	1.23	1.54	3.09	6.17	12.3	24.7
	Re_P (x10^{-2})	0.55	0.69	1.38	2.76	5.52	11.0
	τ_P (min)	2.25	1.80	0.90	0.45	0.23	0.11

Table 2. Porosity, permeability, and tortuosity estimations of the μPBRs.

Reactor	V (μL)	$\emptyset_{RTD}$ (%)	m (mg)	$\emptyset_{mass}$ (%)	κ (mD)	$\mathcal{T}$	r_H (μm)
EμPBR	80.2±0.6	-	0	-	-	1	-
μPBR 1	53.8±0.3	41.3	71.2	40.3	575	1.68	3.37
μPBR 2	52.8±0.4	39.1	73.6	38.3	501	1.73	3.11
μPBR 3	53.5±0.4	40.6	71.7	39.9	557	1.69	3.31
μPBR 4	53.1±0.2	39.7	72.4	39.2	524	1.71	3.23

A μPBR was characterised in order to establish the dimensionless constraints that govern the microfluidic systems *via* RTD measurements. Figs. 3 and S3 show the dimensionless RTDs of the EμPBR and the μPBR. As the flow rates through the EμPBR increased from 10.00 to 40.00μL/min, the mean residence times decreased from 7.97±0.05 to 2.02±0.02 min, and from 5.35±0.03 to 1.35±0.02 min for the μPBR (see Table S1). The variance σ^2 decreased from 2.13 to 0.17 for the

Lab on a Chip Accepted Manuscript

 This journal is © The Royal Society of Chemistry 2014

EμPBR, and it decreased from 1.51 to 0.16 for the μPB (see Table S2). The magnitudes of variances are indications of the "spread" of the distributions. Fig. S3a confirmed the shrinkage. The mean volume obtained from RTD measurements was 80.2±0.6μL for the EμPBR and 53.8±0.3μL for the μPBR, as reported in Table 2 for "μPBR 1". The difference between the two, 26.4μL, corresponds to the volume occupied by quartz particles. The resulting packing efficiency and the porosity of the μPBR were 58.7% and 41.3%, respectively. The corresponding Reynolds number calculated using Equation (9) is reported in Table 1b. As is evident in Table 1, the interstitial velocity within the μPBR was much larger than the mean velocity in the EμPBR for the same volumetric flow rate. Reynolds number in the μPBR ranged from 0.55 to 11.0 x10^{-2} (*i.e.*, < 10), and thus laminar flows were confirmed for residence times ranging from 0.11 to 2.25min.

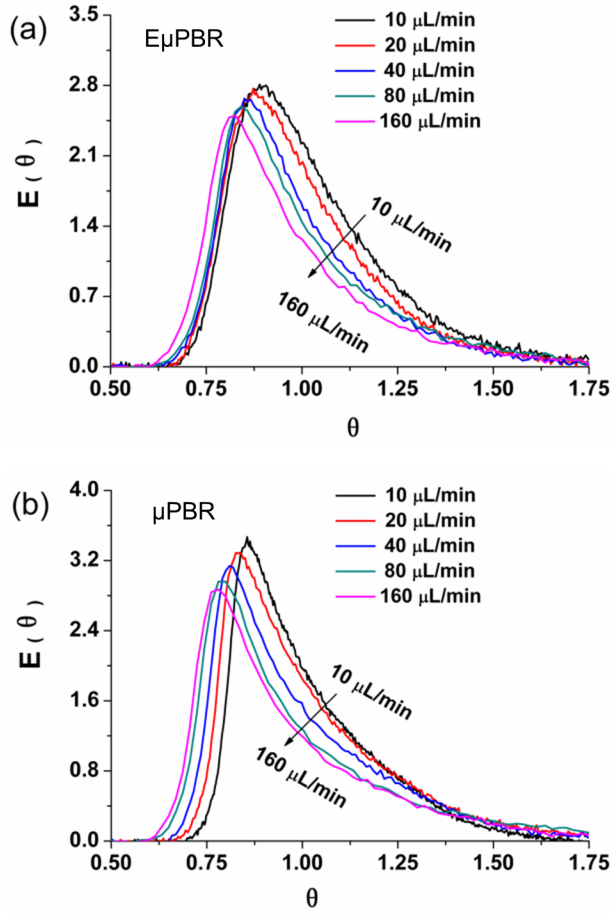

Fig. 3 Residence time distribution measurements of the EμPBR and the μPBR. *E(θ)* values as a function of dimensionless time *(θ)* for (a) the EμPBR and (b) the μPBR. The volumetric flow rates ranged from 10.00 to 160.0μL/min.

The extent of dispersion was evaluated in both the EμPBR and the μPBR. Tracer experiments in *n*-heptane single-phase flows report the dimensionless RTDs of Fig. S3b, which compares *E(θ)* values as a function of dimensionless time *(θ)* for both microreactors given the same velocity of 1.23x10^{-4} m/s. The maximum peak heights of 3.55 (for the μPBR) and 2.73 (for the EμPBR) yield estimations of *(D*/uL)* using Equation (1). As shown in Table S2, *(D*/uL)* is 1.24x10^{-2} within the EμPBR and 7.5x10^{-3} within the μPBR for a velocity of 1.23x10^{-4} m/s. As a consequence, the packing reduced axial dispersion. From Figs. 3a and b, one observes the maximum peak height decreased with increasing volumetric flow rate for both the EμPBR and the μPBR. The corresponding values of *(D*/uL)* are reported in Table S2. From Equation (2), values of $\mathcal{D}$ were calculated to be 0.85x10^{-8} m^2/s (for the EμPBR) and 0.32x10^{-8} m^2/s (for the μPBR), which yielded *Bo* values. Values of *Bo*, ranged from 10 to 10^3 in both the EμPBR and the μPBR, which confirms that convective forces dominated over diffusive forces. One observes in Figs. 3a and b that the maximum peaks shifted left for both the EμPBR and the μPBR as the flow rates increased. Some degree of back-mixing, by dispersion, was likely present within the microreactors[64, 77].

To confirm the reproducibility of the packing efficiency, four μPBR were prepared and the porosities determined by estimations of their RTDs ($\emptyset_{RTD}$). Values of $\emptyset_{RTD}$, ranging from 39.1 to 41.3%, were estimated and reported in Table 2. Quartz masses within each μPBR were also measured, and the corresponding porosity ($\emptyset_{mass}$) estimated from 38.3 to 40.3%. Using Equations (4) and (6), permeability and tortuosity were also estimated to range from 501–575mD and 1.68–1.73, respectively. The resultant diffusivity within μPBs (*i.e.*, 0.32x10^{-8} m^2/s) is less than that within the EμPBR (*i.e.*, 0.85x10^{-8} m^2/s), yet of the same order of magnitude. As shown in Table 2, the hydraulic radii calculated from Equation (7) were ~3.2μm. The preparation of μPBRs with quartz particles was highly reproducible.

The solubility of the asphaltenes and their deposition in μPBRs

As a next step in understanding asphaltene deposition, their solubility in *n*-heptane was measured using inline UV-Vis spectroscopy. The solubility of asphaltenes in *n*-heptane (0 to 90vol%) in toluene was investigated. Mixtures of n-heptane and 4g/L asphaltenes in toluene at varying ratios were stirred and maintained for 24hr at 70.0 ℃ before filtration using Whatman No.3 filter paper. The absorbance of asphaltenes in the filtrates were measured using UV-Vis spectroscopy (at 286nm) and the results shown in Fig. 4 (black squares).

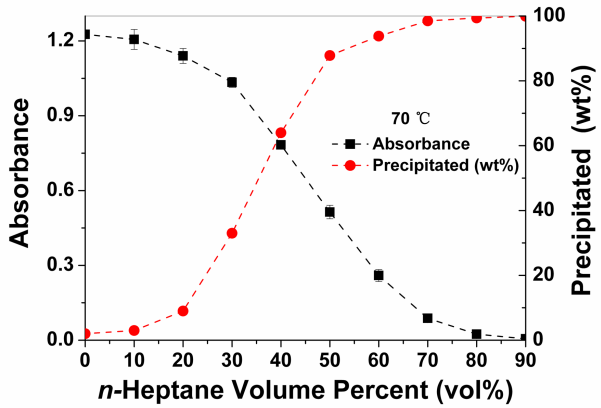

Fig. 4 UV-Vis absorbance of asphaltenes at 286nm in the filtrates, and the corresponding precipitated weight percent of asphaltenes (wt%) for different n-heptane volume fractions (vol%).

Contaminated filter papers were dried and the mass measured. As seen in Fig. 4, the precipitated wt% corresponds to different *n*-heptane volume fractions. The absorbance of asphaltenes

Lab on a Chip Accepted Manuscript

decreased from 1.23 to 5.0x10^{-3} as the volume fraction of *n*-heptane increased from 0 to 90vol%. The precipitated asphaltenes were 93.8wt% for an *n*-heptane volume fraction of 60vol% at 70.0 ℃. The relationship between the anticipated solubility of the asphaltenes for different volume fractions was therefore established, which enabled the design of experiments for asphaltene depositions in μPBRs.

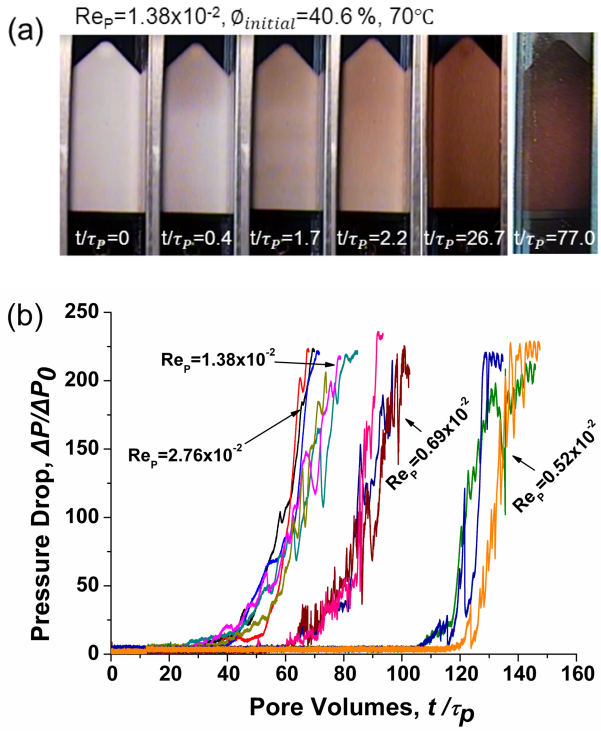

Fig. 5 (a) Photographs of the deposition of asphaltenes in the DμPBRs obtained using a CCD camera for different pore volumes. (b) Influence of the flow rate on the dimensionless pressure drop as a function of the pore volumes of 4g/L asphaltenes in toluene injected.

Depositions of the asphaltenes within μPBRs (*i.e.*, damaged μPBRs, denoted by DμPBRs) were next studied using microscopy. The influence of Reynolds number (Re_P) was investigated in the next set of experiments for constant temperature. Asphaltenes dissolved in toluene (concentration of 4 g/L) and *n*-heptane were delivered into the μPBR at an *n*-heptane concentration of 60vol% for varying total flow rates from 7.50 to 40.00μL/min and Re_P ranging from 0.52 to 2.76x10^{-2}. Fig. 5a shows an example photograph of the deposition of asphatlenes in the DμPBR for different pore volumes (t/τ_P) obtained by CCD camera. Values of Re_P = 1.38x10^{-2} and the initial porosity of 40.6% within the μPBR were estimated. As seen in Fig. 5a, no obvious channelling was observed up to 77.0 pore volumes, as the colour of the DμPBR changed uniformly. Uniform deposition of asphaltenes was observed under these conditions and before plugging.

Analyses of fluidic resistances and μPBR-characterisations further revealed the deposition of the asphaltenes within DμPBRs. Fig. S4 shows the influence of the flow rate on the pressure drop as a function of time, and Fig. 5b illustrates the corresponding dimensionless pressure drop as a function of the pore volumes of 4g/L asphaltenes in toluene injected. One observes in Fig. 5b that Reynolds number influenced the number of pore volumes necessary to obtain dimensionless pressure drop values of 225. The DμPBRs plugged in less pore volumes injected as the ratio of the inertial-to-viscous forces increased. Interestingly, Table 3 shows that as Re_P decreased from 2.76x10^{-2} to 0.52x10^{-2} the mass of asphaltenes deposited increased from 1.1 to 2.1mg. The corresponding damaged porosities were estimated to range from 0.949–0.902 of the original. The porosity of the DμPBR was calculated from the mass of deposited asphaltenes, which was measured by closing the mass balance (*i.e.*, the difference between the mass flow rate of asphaltenes in and out of each DμPBR). The mass of asphaltenes in the waste collector and tubing were also measured by flushing with toluene. Reynolds number clearly plays an important role on the mechanism of asphaltene deposition with μPBRs.

The deposition mechanisms and dispersion within DμPBRs

The mechanism of the deposition process and its impact on permeability impairment are evident upon further evaluation of their relationships to Reynolds number. Statistically, a larger number of asphaltene particles passed through pore throat entrances along stream lines for a given number of pore volumes at larger Re_P compared to smaller Re_P, which ultimately lead to hydrodynamic bridging[78]. At smaller Re_P, precipitated asphaltenes likely penetrated further into DμPBRs and uniformly, resulting in gradual dimensionless pressure drop increases. The porosity loss ($\emptyset_{damage}/\emptyset_{initial}$) of Table 3 was more severe at smaller Re_P under the same dimensionless pressure drop of 225.

Table 3. Influence of Reynolds number on μPBR impairments that generated DμPBRs.

Test	Pore volumes	Re_P (x10^{-2})	$\emptyset_{initial}$	$\kappa_{initial}$ (mD)	m_{total} (mg)	m_{waste} (mg)	$m_{deposited}$ (mg)	$\frac{\emptyset_{damage}}{\emptyset_{initial}}$	$\frac{\kappa_{damage}}{\kappa_{initial}}$	s (x10^3)	$\frac{\Delta P}{\Delta P_0}$
1	68	2.76	39.7±0.6	520±5	4.9	3.8±0.1	1.1	0.949	0.005	3.46	225
2	68	1.38	41.7±0.5	580±4	5.1	4.1±0.2	1.0	0.956	0.004	4.19	134
3	68	0.69	40.7±0.3	556±3	5.0	4.6±0.3	0.4	0.982	0.020	0.85	13
4	68	0.52	40.4±0.7	557±7	5.0	4.8±0.1	0.2	0.991	0.050	0.33	3.7
5	77	1.38	40.6±1.0	560±10	5.5	4.1±0.2	1.4	0.936	0.002	6.86	225
6	77	0.69	40.5±0.6	556±5	5.5	4.9±0.2	0.6	0.973	0.007	2.46	37
7	77	0.52	39.9±0.5	529±5	5.4	5.2±0.2	0.2	0.991	0.048	0.35	3.9
8	96	0.69	40.3±0.6	550±5	7.0	5.3±0.3	1.7	0.922	0.001	12.7	225
9	96	0.52	41.1±0.4	570±3	7.1	6.8±0.2	0.3	0.986	0.045	0.37	4.2
10	115	0.52	40.5±0.3	550±4	8.4	7.1±0.4	1.3	0.941	0.012	3.21	15.3
11	133	0.52	39.7±0.7	524±6	9.5	7.4±0.4	2.1	0.902	0.001	17.2	225

Lab on a Chip Accepted Manuscript

This journal is © The Royal Society of Chemistry 2014

Table 4. Dispersion within μPBR and DμPBRs for different Reynolds numbers.

	u_i (x10^{-4} m/s)	$Re_{P(RTD)}$ (x10^{-2})	σ^2 (min^2)	σ_θ^2	$D^*/(uL)$	D^* (x10^{-8} m^2/s)	Bo
(a)	2.46	0.86	0.85	0.018	0.0086	3.60	90
μPBR	9.84	3.44	0.07	0.023	0.0112	18.8	360
	15.4	5.38	0.04	0.025	0.0120	31.4	563
(b)	2.46	0.86	1.02	0.016	0.0079	3.31	85
DμPBR	9.84	3.44	0.09	0.021	0.0101	16.9	340
	15.4	5.38	0.04	0.024	0.0113	29.6	531

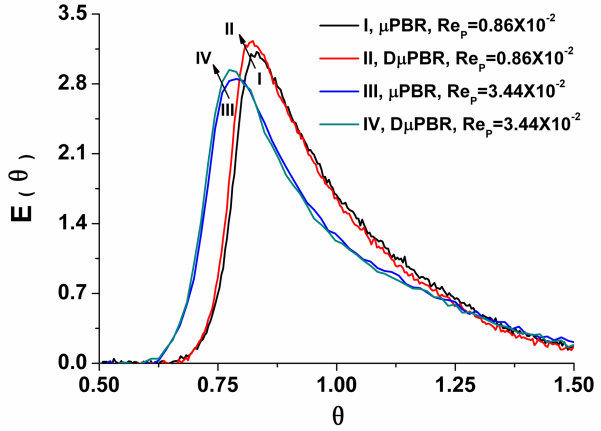

Fig. 6 Comparison of $E(\theta)$ values as a function of dimensionless time (θ) for Reynolds numbers of 0.86x10^{-2} (I and II) and 3.44x10^{-2} (III and IV) within μPBR (I and III) and DμPBRs (II and IV).

Table 3 also reports the permeability impairment ($\kappa_{damage}/\kappa_{initial}$) ranging from 0.001 to 0.058, and the dimensionless Skin Factor of 0.33x10^{-3} to 12.7x10^{3} calculated by Equation (8). The viscosity of the mixture at 70.0 ℃ was obtained from the work of others[73, 74]. Fluctuations of the curves of Fig. 5b at small Re_P of 0.69 and 0.52x10^{-2} are explained by the relationship between the interstitial velocity and the critical velocity necessary to transport desorbed asphaltene particles at quartz particle surfaces. Under such near equilibrium conditions, previously deposited asphaltene particles desorb from quartz surfaces and begin to move with the flow. The pressure drop then increases when the transported asphaltene particles were trapped or absorbed once again on surfaces. The overall deposition process was the combination of asphaltene absorption and desorption and asphaltenes mechanical entrapment[47]. Larger relative ratios of the inertia to the viscous forces favour mechanical entrapment

Analyses of RTDs of DμPBRs and their comparison to μPBRs reveal the influence of impairments on axial dispersion. The RTDs of DμPBRs were measured after injecting 115 pore volumes for Re_P of 0.52x10^{-2}. Fig. S5 shows the RTDs of the EμPBR, μPBR, and DμPBRs. One observes in Fig. S5a that the maximum absorbance of a DμPBR shifted left by comparison of the values of the μPBR, which is attributed to the deposition of asphaltenes. The difference in mean volumes between the μPBR (53.5±0.4μL) and the DμPBR (52.5±0.3μL) was 1.0μL, which corresponds to $\emptyset_{damage}/\emptyset_{initial}$ values of 94.5%. The result was also approximated from the mass accumulated of 1.3 mg, which corresponds to a volume decrease of ~1.1μL and $\emptyset_{damage}/\emptyset_{initial}$ values of 94.5%. Figure 6 and Table 4 demonstrate that in general axial dispersion increased with increasing $Re_{P(RTD)}$ values. The same trend was observed for $Re_{P(RTD)}$ values ranging from 0.86x10^{-2} to 3.44x10^{-2} for μPBRs (I and III) and DμPBRs (II and IV), separately. For a given $Re_{P(RTD)}$, however, axial dispersion was reduced by the deposition of the asphaltenes at 70.0 ℃. No significant channeling was observed in DμPBRs, as illustrated by the single mode of Figure 6 (*i.e.*, the by-bass model does not accurately describe the system)[66]. The design of μPBRs, their characterization, and integration with online analytics lay the groundwork for understanding nanofluidic by-pass pore throat models that predict DμPBRs. Such information is ubiquitous towards revealing the relationship of the two deposition mechanisms and the dimensionless constraints that describe macroscale scenarios.

Conclusions

The deposition of asphaltenes in porous media, an important problem in science and macromolecular engineering, was for the first time investigated in transparent packed-bed microreactors with online analytics to generate high-throughput information. Highly reproducible, stable packings of quartz particles with porosity of ~40% and permeability of ~500mD were designed. The presence of the quartz particles reduced axial dispersion under the same velocity *via* estimations of the dispersion coefficients and the Bodenstein number. The deposition of asphaltenes decreased axial dispersion.

The high-throughput chemical and microfluidic information revealed the influence of Reynolds number on asphaltene deposition within packed-bed microreactors. For low Reynolds numbers, evidence of asphaltene adsorption onto quartz particle surfaces was revealed. For larger Reynolds numbers, mechanical entrapment likely resulted in significant pressure drops for less pore volumes injected and less mass of asphaltenes being retained under the same maximum dimensionless pressure drop. In general, the mass of asphaltenes deposited increased as Reynolds number decreased for the same pore volumes injected. As a consequence, the corresponding porosity loss increased and the permeability decreased. No significant channelling was evident in any scenario. The innovation of packed-bed microfluidics for investigations on asphaltene deposition mechanisms promises to contribute to society by bridging macromolecular science with microsystems.

Acknowledgements

We gratefully acknowledge Nalco Energy Services and Anadarko Petroleum Corporation for funding. Brian S. Flowers also graciously helped create files using AutoCAD.

Lab on a Chip Accepted Manuscript

Notes and references

Department of Chemical and Biological Engineering, The University of Alabama, Box 870203, Tuscaloosa, AL 35487, USA; E-mail: rhartman@eng.ua.edu

† Electronic Supplementary Information (ESI) available. See DOI: 10.1039/b000000x/

1. O. C. Mullins, E. Y. Sheu, A. Hammami, A.G. Marshall, *Asphaltenes, Heavy Oils, and Petroleomics*, Springer, New York, 2007.
2. O. C. Mullins, *Energy Fuels,* 2010, 24, 2179-2207.
3. J. P. Dickie and T. F. Yen, *Anal. Chem.,* 1967, **39**, 1847-1852.
4. O. C. Mullins, *SPE J*., 2008, **13**, 48-57.
5. D. D. Li and M. L. Greenfield, *Energy Fuels,* 2011, **25**, 3698-3705.
6. O. C. Mullins, H. Sabbah, J. Eyssautier, A. E. Pomerantz, L. Barre, A. B. Andrews, Y. Ruiz-Morales, F. Mostowfi, R. McFarlane, L. Goual, R. Lepkowicz, T. Cooper, J. Orbulescu, R. M. Leblanc, J. Edwards and R. N. Zare, *Energy Fuels*, 2012, **26**, 3986-4003.
7. S. Sabbaghi, M. Shariaty-Niassar, S. Ayatollahi and A. Jahanmiri, *J. Microscopy*, 2008, **231**, 364-373.
8. J. Eyssautier, P. Levitz, D. Espinat, J. Jestin, J. Gummel, I. Grillo and L. Barre, *J. Phys. Chem. B*, 2011, **115**, 6827-6837.
9. Y. Bouhadda, D. Bormann, E. Sheu, D. Bendedouch, A. Krallafa and M. Daaou, *Fuel,* 2007, **86**, 1855-1864.
10. R. D. Cadena-Nava, A. Cosultchi and J. Ruiz-Garcia, *Energy Fuels*, 2007, **21**, 2129-2137.
11. M. Sedghi, L. Goual, W. Welch and J. Kubelka, *J. Phys. Chem. B*, 2013, **117**, 5765-5776.
12. L. Y. Zhang, P. Breen, Z. H. Xu and J. H. Masliyah, *Energy Fuels*, 2007, **21**, 274-285.
13. L. Y. Zhang, R. Lopetinsky, Z. Xu and J. H. Masliyah, *Energy fuels*, 2005, **19**, 1330-1336.
14. M. Jeribi, B. Almir-Assad, D. Langevin, I. Henaut and J. Argillier, *J. Colloid Interface Sci.,* 2002, **256**, 268-272.
15. J. P. Rane, V. Pauchard, A. Couzis and S. Banerjee, *Langmuir,* 2013, **29**, 4750-4759.
16. P. M. Spiecker, K. L. Gawrys and P. K. Kilpatrick, *J. Colloid Interface Sci.,* 2003, **267**, 178-193.
17. D. L. Mitchell and J. G. Speight, *Fuel,* 1973, **52**, 149-152.
18. J. Murgich, D. Merino-Garcia, S. I. Andersen, J. M. del Rio and C. L. Galeana, *Langmuir,* 2002, **18**, 9080-9086.
19. T. Maqbool, S. Raha, M. P. Hoepfner and H. S. Fogler, *Energy Fuels*, 2011, **25,** 1585-1596.
20. I. N. Evdokimov, N. Y. Eliseev and B. R. Akhmetov, *J.Pet. Sci. Eng.*, 2003, **37**, 135-143.
21. I. N. Evdokimov, N. Y. Eliseev and B. R. Akhmetov, *J.Pet. Sci. Eng.*, 2003, **37**, 145-152.
22. E. Rogel, *Energy Fuels*, 2000, **14**, 566-574.
23. F. Arteaga-Larios, A. Cosultchi and E. Perez, *Energy Fuels*, 2005, **19**, 477-484.
24. F. Mostowfi, K. Indo, O. C. Mullins and R. McFarlane, *Energy Fuels*, 2009, **23**, 1194-1200.
25. I. A. Wiehe, *Energy Fuels*, 2012, **26**, 4004-4016.
26. S. Acevedo, M. A. Ranaudo, C. Garcia, J. Castillo, A. Fernandez, M. Caetano and S. Goncalvez, *Colloids Surf.,A-Physicochemical and Engineering Aspects,* 2000, **166**, 145-152.
27. M. P. Hoepfner, V. Limsakoune, V. Chuenmeechao, T. Maqbool and H. S. Fogler, *Energy Fuels*, 2013, **27**, 725-735.
28. J. X. Wang, J. S. Buckley and J. L. Creek, *J. Dispersion Sci. Technol.*, 2004, **25**, 287-297.
29. R. Aveyard, J. H. Clint, D. Nees and V. N. Paunov, *Langmuir*, 2000, **16**, 1969-1979.
30. S. Verdier, F. Plantier, D. Bessieres, S. I. Andersen, E. H. Stenby and H. Carrier, *Energy Fuels*, 2007, **21**, 3583-3587.
31. T. Maqbool, P. Srikiratiwong and H. S. Fogler, *Energy Fuels*, 2011, **25**, 694-700.
32. A. W. Marczewski and M. Szymula, *Colloids Surf., A-Physicochemical and Engineering Aspects,* 2002, **208**, 259-266.
33. N. B. Joshi, O. C. Mullins, A. Jamaluddin, J. Creek and J. McFadden, *Energy Fuels*, 2001, **15**, 979-986.
34. S. Peramanu, C. Singh, M. Agrawala and H. W. Yarranton, *Energy Fuels*, 2001, **15**, 910-917.
35. J. S. Buckley, *Energy Fuels*, 2012, **26**, 4086-4090.
36. A. Hammami, C. H. Phelps, T. Monger-McClure and T. M. Little, *Energy Fuels*, 2000, **14**, 14-18.
37. S. A. Mousavi Dehgani, M. Vafaie Sefti, B. Mirzayi and M. Fasih, -*Int. Eng. Edit*., 2007, **26**, 39-48.
38. E. S. Boek, A. D. Wilson, J. T. Padding, T. F. Headen and J. P. Crawshaw, *Energy Fuels*, 2009, **24**, 2361-2368.
39. E. S. Boek, H. K. Ladva, J. P. Crawshaw and J. T. Padding, *Energy Fuels*, 2008, **22**, 805-813.
40. T. J. Kaminski, H. S. Fogler, N. Wolf, P. Wattana and A. Mairal, *Energy Fuels,* 2000, **14**, 25-30.
41. L. Carbognani, *Energy fuels*, 2001, **15**, 1013-1020.
42. P. Permsukarome, C. Chang and H. S. Fogler, *Ind. Eng. Chem. Res*., 1997, **36**, 3960-3967.
43. C. A. Franco, N. N. Nassar, M. A. Ruiz, P. Pereira-Almao and F. B. Cortes, *Energy Fuels*, 2013, **27**, 2899-2907.
44. J. Gummel, Y. Corvis, J. Jestin, J. M'Hamdi and L. Barre, *Eur. Phys.J.-Special Topics*, 2009, **167**, 171-176.
45. S. S. Datta, H. Chiang, T. Ramakrishnan and D. A. Weitz, *Phys. rev. lett.*, 2013, **111**, 064501.
46. I. Kocabas, M. R. Islam and H. Modarress, *J. Pet. Sci. Eng.*, 2000, **26**, 19-30.
47. R. A. Almehaideb, *J. Pet. Sci. Eng.*, 2004, **42**, 157-170.
48. L. Nabzar, M. Aguilera and Y. Rajoub, J. *SPE*, 2005.
49. G. Fung, W. Backhaus, S. McDaniel, M. Erdogmus and B. America, *OTC*, 2006.
50. M. W. Losey, M. A. Schmidt and K. F. Jensen, *Ind. Eng. Chem. Res.*, 2001, **40**, 2555-2562.
51. K. F. Jensen, *Chem. Eng. Sci.*, 2001, **56**, 293-303.
52. N. Marquez, P. Castano, M. Makkee, J. A. Moulijn and M. T. Kreutzer, *Chem. Eng. Technol.*, 2008, **31**, 1130-1139.
53. M. H. Schneider, V. J. Sieben, A. M. Kharrat and F. Mostowfi, *Anal. chem.*, 2013, **85**, 5153-5160.
54. R. Fisher, M. K. Shah, D. Eskin, K. Schmidt, A. Singh, S. Molla and F. Mostowfi, *Lab Chip*, 2013, **13**, 2623-2633.
55. M. Kim, A. Sell and D. Sinton, *Lab Chip*, 2013, **13**, 2508-2518.56. T. W. de Haas, H. Fadaei, U. Guerrero and D. Sinton, *Lab Chip*, 2013, **13**, 3832-3839.
57. S. A. Bowden, R. Wilson, J. Parnell and J. M. Cooper, *Lab Chip*, 2009, **9**, 828-832.

Lab on a Chip Accepted Manuscript

 This journal is © The Royal Society of Chemistry 2014

58. R. L. Hartman, J. R. Naber, S. L. Buchwald and K. E. Jensen, *Angew. Chem., Int. Ed.*, 2010, **49**, 899-903.
59. R. L. Hartman and K. F. Jensen, *Lab Chip*, 2009, **9**, 2495-2507.
60. R. L. Hartman, H. R. Sahoo, B. C. Yen and K. F. Jensen, *Lab Chip*, 2009, **9**, 1843-1849.
61. R. L. Hartman, J. R. Naber, N. Zaborenko, S. L. Buchwald and K. F. Jensen, *Org. Process Res. Dev.*, 2010, **14**, 1347-1357.
62. C. Hu, C. Herz, and R. L. Hartman, *Green Process Synth*, 2013, **2**, 611-623.
63. K. B. van Gelder and K. R. Westerterp, *Chem. Eng. Technol.*, 1990, **13**, 27-40.
64. O. Levenspiel, *Chemical Reaction Engineering*, 3rd edition, 1999.
65. V. Sans, N. Karbass, M. I. Burguete, E. García-Verdugo and S. V. Luis, *RSC Adv.*, 2012, **2**, 8721-8728.
66. H. S. Fogler, *Elements of Chemical Reaction Engineering*, 1999.
67. S. Whitaker, *Trans. Porous Media*, 1986, **1**, 3-25.
68. F. Lucia, *J. Pet. Technol.*, 1983, **35**, 629-637.
69. M. Yun, B. Yu, P. Xu and J. Wu, *Can. J. Chem. Eng.,* 2006, **84**, 301-309.
70. L. Shen and Z. Chen, *Chem. Eng. Sci.,* 2007, **62**, 3748-3755.
71. K. Leontaritis, *SPE J.*, 1998, 277-288.
72. M. Rhodes, *Introduction to particle technology*, Wiley, 2008.
73. I. Abdulagatov and S. Rasulov, *Berichte der Bunsengesellschaft für physikalische Chemie*, 1996, **100**, 148-154.
74. M. Assael, N. Dalaouti and J. Dymond, *Int. J. Thermophys.*, 2000, **21**, 291-299.
75. H. Kashiwagi, T. Hashimoto, Y. Tanaka, H. Kubota and T. Makita, *Int. J. Thermophys.*, 1982, **3**, 201-215.
76. A. J. Queimada, S. Quinones-Cisneros, I. M. Marrucho, J. A. Coutinho and E. H. Stenby, *Int. J. Thermophys.*, 2003, **24**, 1221-1239.
77. K. D. Nagy, Massachusetts Institute of Technology, Department of Chemical Engineering, 2012.
78. V. Ramachandran and H. S. Fogler, *J. Fluid Mech.,* 1999, **385**, 129-156.

Lab on a Chip Accepted Manuscript